IEEE Photonics Journal
An IEEE Photonics Society Publication

Asymmetrical Fiber Mach–Zehnder Interferometer for Simultaneous Measurement of Axial Strain and Temperature

Volume 2, Number 6, December 2010

Ping Lu
Qiying Chen

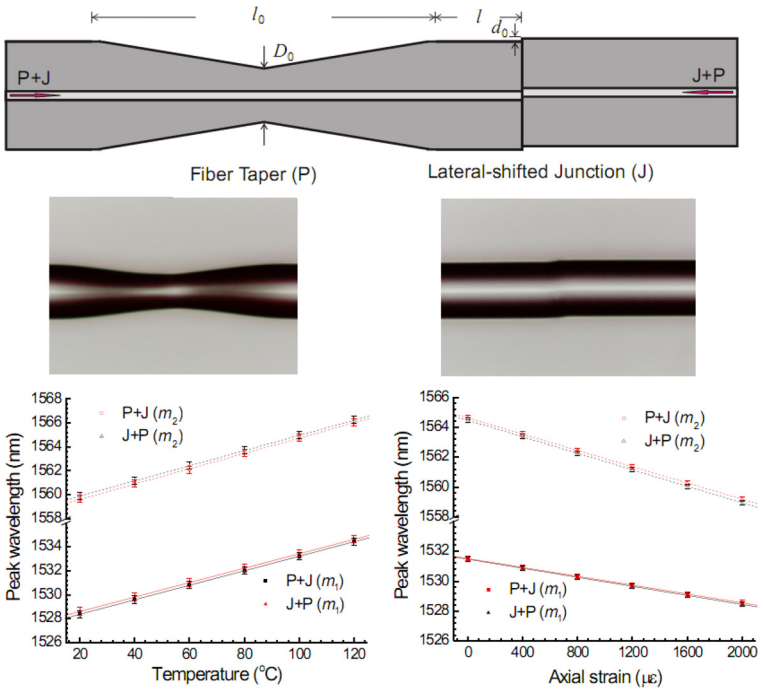

DOI: 10.1109/JPHOT.2010.2082513
1943-0655/$26.00 ©2010 IEEE

Asymmetrical Fiber Mach–Zehnder Interferometer for Simultaneous Measurement of Axial Strain and Temperature

Ping Lu[1] **and Qiying Chen**[1,2]

[1]Department of Physics and Physical Oceanography, Memorial University of Newfoundland, St. John's, NF A1B 3X7, Canada
[2]Faculty of Engineering and Applied Science, Memorial University of Newfoundland, St. John's, NF A1B 3X5, Canada

DOI: 10.1109/JPHOT.2010.2082513
1943-0655/$26.00 ©2010 IEEE

Manuscript received August 26, 2010; revised September 21, 2010; accepted September 23, 2010. Date of publication September 30, 2010; date of current version October 15, 2010. This work was supported by the Natural Sciences and Engineering Research Council of Canada, Canada Research Chairs Program, Canada Foundation for Innovation, the Province of Newfoundland and Labrador, and the Memorial University of Newfoundland. Corresponding author: Q. Chen (e-mail: qiyingc@mun.ca).

Abstract: An asymmetrical fiber Mach–Zehnder interferometer (aFMZI) consisting of a fiber taper and a lateral-shifted junction is proposed and demonstrated to realize simultaneous measurement of axial strain and temperature. The interferometer exhibits different environmental sensitivities for different device architectures. If the taper and the lateral-shifted junction locate spatially close (15 mm), the experimental results would indicate temperature sensitivities of 60.4 and 63.9 pm/°C (redshift) and axial strain sensitivities of -1.47 and -2.71 pm/$\mu\varepsilon$ (blueshift) at the higher and lower interference orders m_1 (49) and m_2 (48), respectively, for the taper–junction interferometer. The junction–taper interferometer has temperature sensitivities of 60.1 and 63.3 pm/°C (redshifts) and axial strain sensitivities of -1.51 and -2.75 pm/$\mu\varepsilon$ (blueshifts) at the interference orders m_1 and m_2, respectively.

Index Terms: Sensors, fiber optics systems.

1. Introduction

Simultaneous measurement of strain and temperature is of great importance for many applications, for example, nondestructive evaluation of civil infrastructure, structure inspection of aircraft, spacecraft, automobiles, and ships, as well as environmental monitoring, including earthquake and volcano surveillance. A wide variety of optical fiber-based sensing techniques have been proposed to meet such requirements owing to their unique advantages such as immunity to electromagnetic interference, compact size, potential low cost, and the possibility of distributed measurement over a long distance [1]. Among different fiber-optic techniques, fiber Mach–Zehnder interferometers (FMZIs) exhibit salient merits of high sensitivity, a high degree of integration, simplicity, and compact in-line measurement, with wealthy physical mechanisms for applications ranging from waveguide, routing, filtering, and nonlinear optical probing to sensing [2]–[5]. FMZIs reported so far can be classified into two categories: the symmetrical fiber Mach–Zehnder interferometer (sFMZI) and the asymmetrical fiber Mach–Zehnder interferometer (aFMZI). Reported sFMZIs include four single-mode fiber splitters with strictly defined beam-splitting ratios [6], mechanically induced two identical

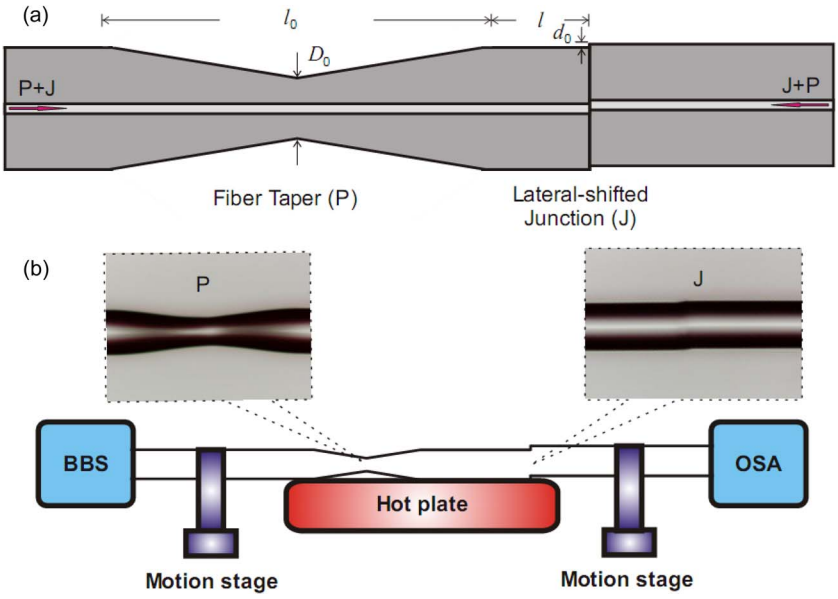

Fig. 1. (Color online) (a) Schematic illustration of the fiber device developed in this study, (b) experimental setup with the left and right insets showing the optical micrographs of the fiber taper (P) and the lateral-shifted junction (J) in the interferometer, respectively.

long-period fiber gratings (LPGs) in a photonic crystal fiber (PCF) [7], a fiber-taper section between an LPG pair [8], spliced two pieces of a PCF with a small lateral offset or collapsed air-holes of a single PCF [9], two core-offset attenuators on a single-mode fiber [10], two tandem fiber tapers by fusion splicing [11]–[13], a single abrupt taper in a single-mode fiber with a fiber end of an air-glass interface or gold coating [14], [15], and two points on a single-mode fiber by CO_2 laser irradiations [16]. The reported aFMZIs include a fiber multimode interferometric structure combined with a LPG [17], a nonadiabatic taper cascaded with an LPG [18], and interaction of a misaligned fusion-spliced point with an LPG on a single-mode fiber [19] or on a PCF [20]. The FMZIs reported so far usually involve highly demanding fiber grating fabrication techniques, critical requirements on interferometer specifications (two identical LPGs or fiber tapers, alignment of two core-offsets), or the use of high-cost PCFs, which restrict their practical applications. In this paper, an in-line one-fiber approach to realize simultaneous measurement of axial strain and temperature is proposed and experimentally demonstrated. Two aFMZIs with different device architectures consisting of a fiber taper and a lateral-shifted junction are fabricated in a single-mode fiber using the electrical arc method. Different gradients of the attenuation peak wavelengths on axial strain and temperature for the two types of aFMZI at two interference orders will be investigated to demonstrate the effectiveness of the approach.

2. Device Structure Analysis and Simulation

Fig. 1(a) shows a schematic illustration of an optical fiber device with a distance of *l* between a fiber taper (P) and a lateral-shifted junction (J). The abrupt fiber taper was shaped by tapering a standard telecommunication single-mode optical fiber (SMF-28e, Corning Inc.) using a fusion splicer (FITEL S182A). The fiber fixed on two aligned holding plates was stretched, and the middle region was heated by arc from the two electrodes inside the fusion splicer. The fiber was sharpened to a waist diameter D_0 of 75 μm with a taper length l_0 of 470 μm, as shown in the left inset of Fig. 1(b). To fabricate a lateral-shifted junction from two off-centered fiber cores, two pre-aligned fibers with a designed lateral shift were fusion-spliced using the electrical arc method. The right inset of Fig. 1(b) displays the optical micrograph of the lateral-shifted junction with a fiber core offset d_0 of 5 μm. Fig. 1(b) shows that light emitted from an erbium broadband light source (EBS-7210, MPB

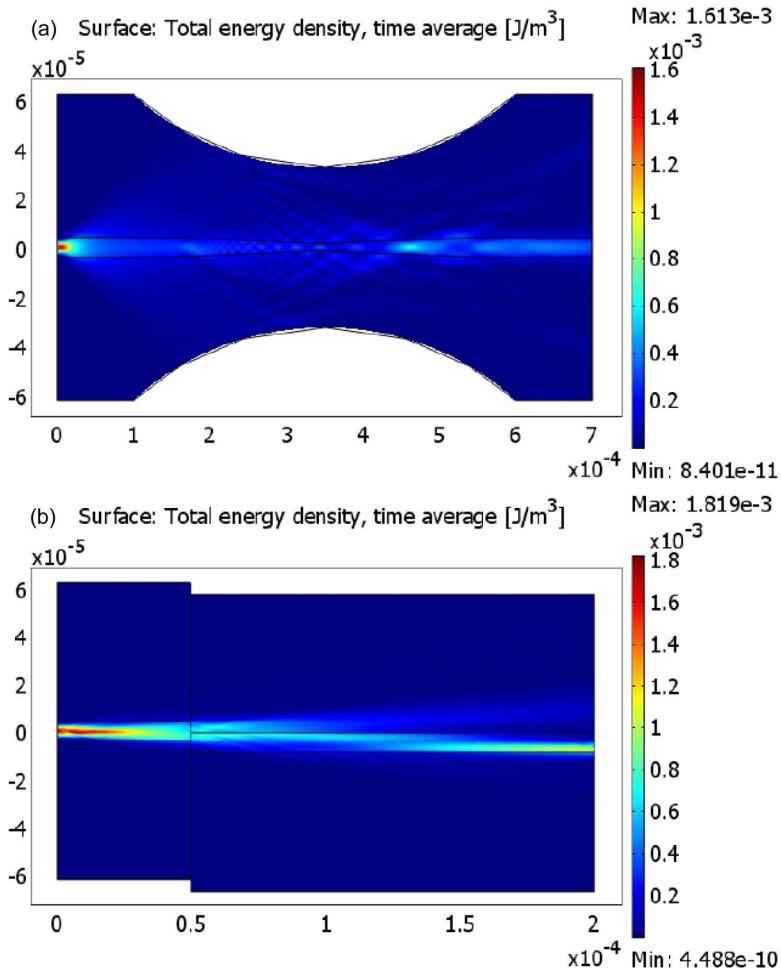

Fig. 2. Simulation of light energy density distribution along (a) a fiber taper ($D_0 = 70\ \mu$m, $l_0 = 500\ \mu$m) and (b) a lateral-shifted junction ($d_0 = 5\ \mu$m) at $\lambda = 1.55\ \mu$m.

Communications, Inc.) is monitored by an optical spectrum analyzer (OSA, Ando 6315E) after passing through the fiber device. Light propagates through a fiber taper followed by a lateral-shifted junction is defined as an aFMZI of taper–junction type $(\mathrm{P} + \mathrm{J})$, and accordingly, an aFMZI of junction–taper type $(\mathrm{J} + \mathrm{P})$ is defined as light transmission through a lateral-shifted junction and a fiber taper in sequence.

In order to verify the incident light energy propagation and the coupling effect, a 2-D finite element analysis has been used to simulate both the fiber taper and the lateral-shifted junction with the results presented in Fig. 2. For the fiber taper, excitation energy of LP_{01} in fiber core mode will be partly coupled to high-order LP_{0n} cladding modes at the beginning of the fiber taper region [see Fig. 2(a)]. Similarly, part of the core mode energy also leaks to cladding modes at the junction position for the lateral-shifted junction [Fig. 2(b)]. An aFMZI will be formed when part of the light energy in the fiber core is coupled into the cladding by the first taper (or junction), and the second junction (or taper) couples the cladding mode energy back into the core after passing through a spatial separation between them.

In order to investigate the influence of structure parameters on the device performance, fiber tapers with different ratios of taper length to waist diameter from 700 μm/35 μm, 580 μm/60 μm to 400 μm/95 μm and lateral-shifted junctions with different core offsets of 2, 4, and 6 μm were fabricated. Fig. 3(a) shows the attenuation spectra of these different structures. It indicates that the attenuation will increase when the ratio of taper length to waist diameter increases or the core offset

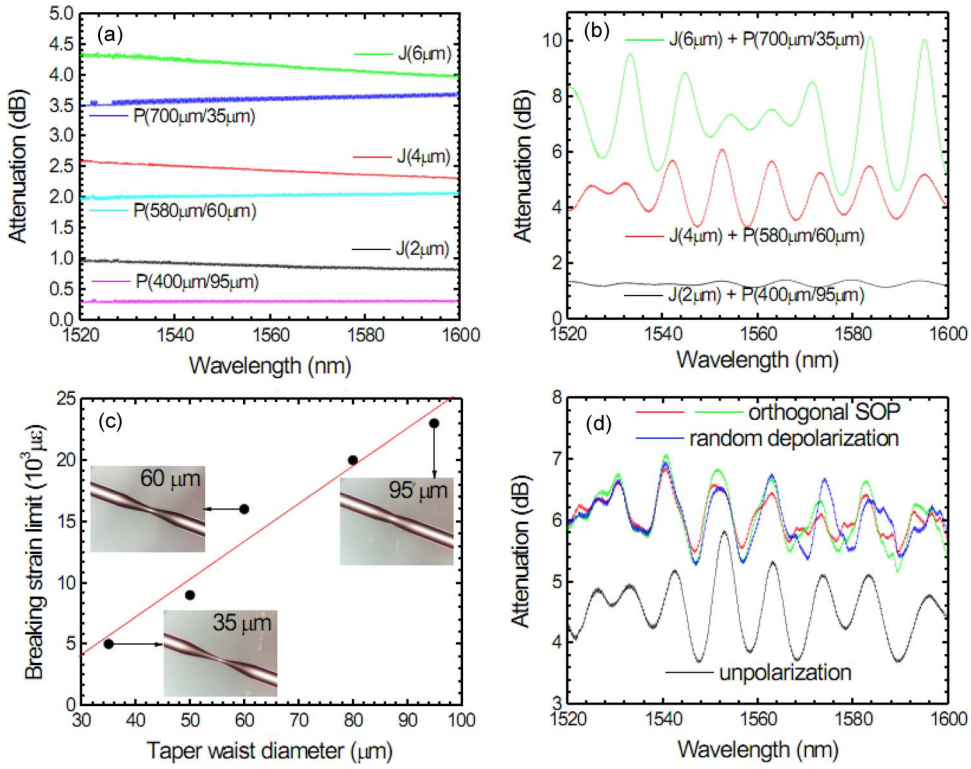

Fig. 3. (a) Attenuation spectra of single fiber tapers (P) with different length/diameter ratios (l_0/D_0) and single lateral-shifted junctions (J) with different parameters (d_0), (b) attenuation spectra of J + P type aFMZIs with different parameters, (c) the dependences of breaking strain limit on the waist diameter of the fiber taper, and (d) attenuation spectra of the aFMZI of J(4 μm) + P(580 μm/60 μm) at different SOP.

expands. For the taper (700 μm/35 μm) in the wavelength range of 1520 to 1600 nm, the minimal attenuation of 3.51 dB occurs at 1520 nm, and the largest attenuation of 3.79 dB appears at 1600 nm because the mode field diameter (MFD) decreases with the decreasing wavelength, and less energy is coupled from the core mode to the cladding modes at shorter wavelength region. In contrast, a rise in the attenuation spectrum of the lateral-shifted junction is observed. For the junction of $d_0 = 6$ μm, the attenuation of 4.29 dB at a wavelength of 1520 nm decreases to 3.95 dB at 1600 nm with an attenuation difference of 0.34 dB. This is also due to the change in MFD while less energy is transferred between the two core modes, and the loss is greater at a shorter wavelength. Fig. 3(b) shows the attenuation spectra of J + P type aFMZIs with the combinations of these structure parameters. It is indicated that the aFMZI consisting of a longer and slimmer taper and a more misaligned junction has a higher extinction ratio [e.g., 6 dB for J(2 μm) + P(700 μm/35 μm)] than the combinations of a shorter and thicker taper with a little lateral-shifted junction [e.g., 3 dB for J(4 μm) + P(580 μm/60 μm) and 0.5 dB for J(2 μm) + P(730 μm/35 μm)]; nevertheless, it suffers a larger attenuation [e.g., 7 dB for J(2 μm) + P(700 μm/35 μm)] simultaneously. Fig. 3(c) shows the dependence of the breaking strain limit on the waist diameter of the fiber taper, indicating that any decrease in the waist diameter of the fiber taper may reduce the mechanical strength of the fiber from a breaking strain limit of 23×10^3 $\mu\varepsilon$ for the taper of $d_0 = 95$ μm to 5×10^3 $\mu\varepsilon$ for the taper of $d_0 = 35$ μm. A taper with a waist diameter of 75 μm and a junction core offset of 5 μm was chosen for the sensing experiment because it achieves good interferometric pattern of reasonable extinction ratio as well as adequate mechanical strength to withstand damage from fabrication, packaging, and practical sensing applications. As it will be clear in the next section, the sensing with the aFMZIs in this study is achieved through the monitoring of the wavelength shift of the interferometric pattern, and the extinction ratio of the device is not crucial for the sensing as long as

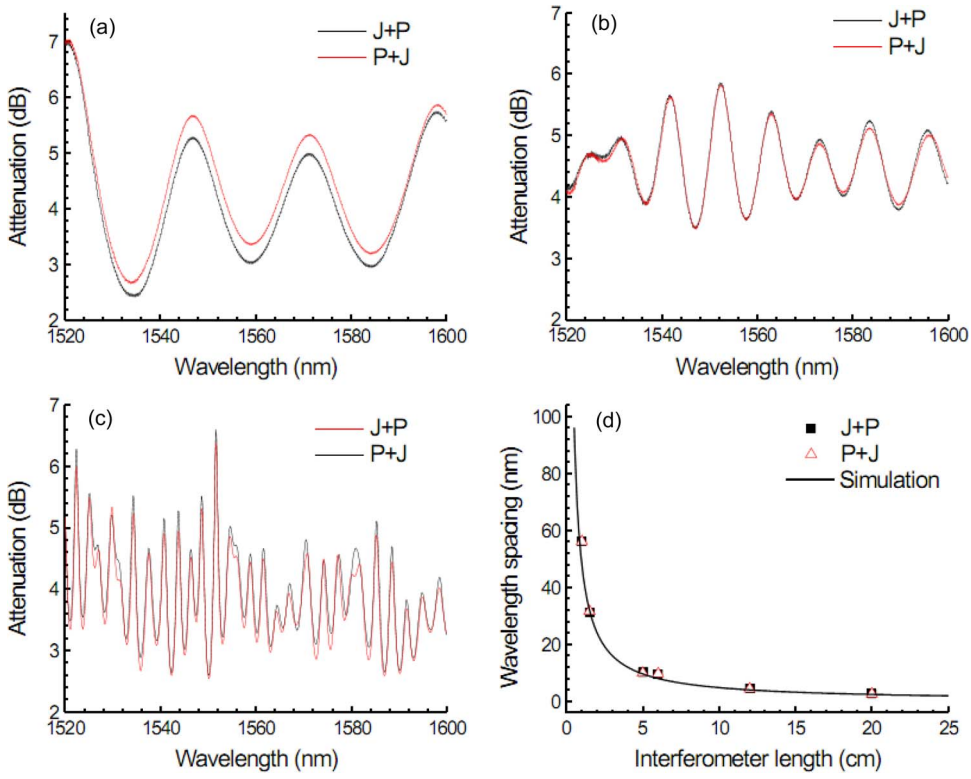

Fig. 4. Attenuation spectra of J + P and P + J type aFMZIs with different interferometer lengths. (a) 2 cm, (b) 5 cm, (c) 20 cm, and (d) the dependence of wavelength spacing on the interferometer length for the two types of aFMZI.

an interferometric pattern is detectable. Fig. 3(d) shows the attenuation spectra of the aFMZI of J(4 μm) + P(580 μm/60 μm) with different incident polarization states (SOP) of orthogonal, random depolarized, and unpolarized polarization states modulated by a polarization controller (HP 11896A). It is indicated that the wavelength spacing and extinction ratio are closely related with the disturbance by polarization modulation. The polarization dependence of the aFMZI is mainly due to the refractive index difference between the core and cladding mode, which is polarization dependent, and thus, the phase difference is distinct in despite of a constant interferometer length.

The phase difference Φ between the core mode and the cladding modes can be expressed as $\Phi = 2\pi\Delta n_{\text{eff}} L/\lambda$, where Δn_{eff} is the difference of the effective refractive indices between the core mode and the cladding modes, L is the length of the interferometer, and λ is the operation wavelength. When the phase difference satisfies the condition $\Phi = (2m + l)\pi$, where m is the order of the Mach–Zehnder interference, the attenuation peak wavelength λ_m can be found at $\lambda_m = 2\Delta n_{\text{eff}} L/(2m + 1)$, with an interference order m. The center peak wavelength is related to the mode coupling regions (P + J or J + P) through the multiplication of Δn_{eff} and L. Since the mechanism of the aFMZIs reported here is the Mach–Zehnder interferometry, which is determined by the phase difference between the light beams propagating through the fiber core and cladding, the properties between the taper (P) and the junction (J), such as Δn_{eff} and L, are crucial but not other details of the taper or the junction. The wavelength spacing between the adjacent attenuation peak wavelengths $\Delta\lambda_m$ is $\Delta\lambda_m = 4\Delta n_{\text{eff}} L/(2m + 1)(2m - 1) \approx \lambda_m^2/(\Delta n_{\text{eff}} L)$, if $m \gg 1$. The relation between the wavelength spacing and the interferometer length is shown in Fig. 4, in which (a), (b), and (c) are the attenuation spectra of the J + P and P + J type aFMZIs of J(4 μm) + P(580 μm/60 μm) with different interferometer lengths of 2, 5, and 20 cm, respectively. Fig. 4(d) indicates that the wavelength spacing is inversely proportional to the distance between the fiber taper and the lateral-shifted junction, and the experimental results are consistent with the simulation. The differences in

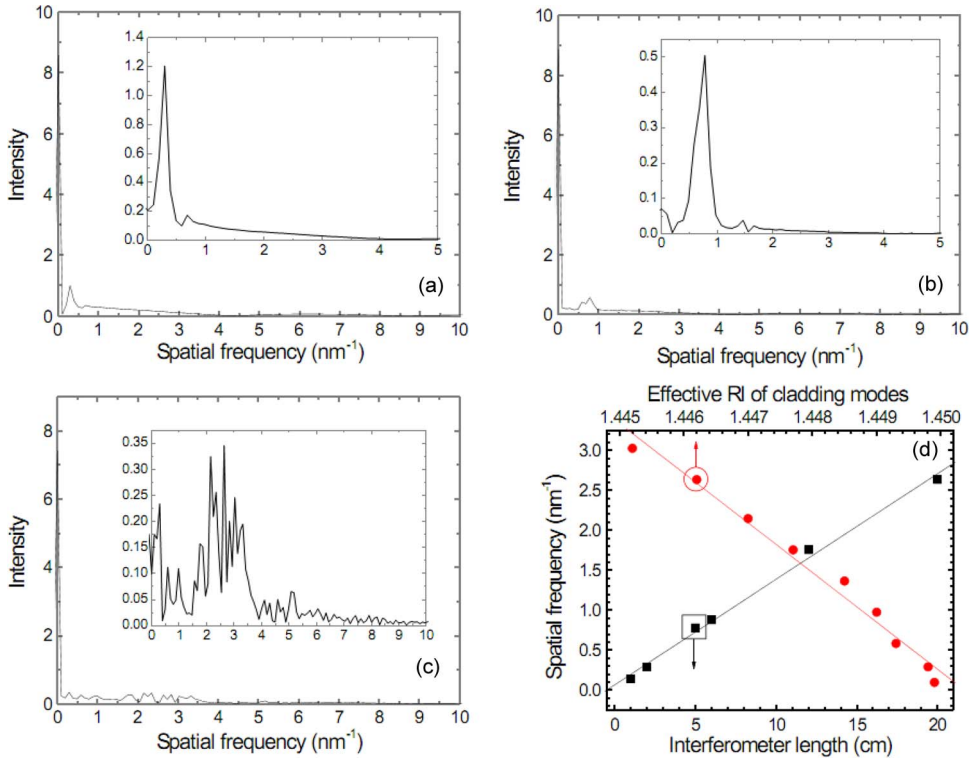

Fig. 5. Spatial frequency spectra of J + P type aFMZIs with different interferometer lengths. (a) 2 cm, (b) 5 cm, (c) 20 cm, and (d) the dependences of spatial frequency on the interferometer length and cladding mode effective refractive index (RI) for the aFMZI of 20 cm in length.

the effective refractive index of the P + J type aFMZI are calculated to be 0.004376 from the simulated results and that of the J + P type aFMZI as 0.004382 at a wavelength of 1530.00 nm. To study the energy distribution in the lower order cladding modes, the wavelength spectra of P + J type aFMZI in Fig. 4(a)–(c) are Fourier transformed to obtain the spatial frequency spectra of the interference fringes [9]. The dominant intensity peaks at zero spatial frequency in Fig. 5(a)–(c) relate to the core modes of the three J + P type aFMZIs with different lengths. The multiple minor intensity peaks in the insets of Fig. 5(a)–(c) correspond to different orders of cladding modes of three aFMZIs. For the 20-cm aFMZI in the inset of Fig. 5(c), a series of intensity peaks are obvious in the spatial frequency spectrum, and the sixth and the seventh have the highest peaks among them, which indicate that these two orders of cladding modes have the largest energies after passing through the junction and taper region. Fig. 5(d) shows that the spatial frequencies of the corresponding minor peaks are proportional to the effective refractive indices of the lower order cladding modes for the same interferometer length *L* of 20 cm aFMZI in the inset of Fig. 5(c). Meanwhile, the figure also indicates that the spatial frequencies of the dominant peaks in the insets of Fig. 5 are proportional to the interferometer length, which means that the mode coupling of different aFMZIs mainly occurs at the same orders of cladding modes of LP_{07} or LP_{08}.

3. Sensing Applications

For the measurement of the temperature (T) and axial strain (ε) with the aFMZI, the optical fiber was axially stretched at different temperatures controlled by a Sigma system with a temperature accuracy of 0.1 °C. The aFMZI was fixed on two linear motion stages (ATS100, Aerotech, Inc.) using epoxy glue, and the length of the fiber segment containing a 15-mm-long aFMZI of J(5 μm) + P(470 μm/75 μm) between the two fixed points was 330 mm. The axial strain was adjusted with the motion stage with a translation accuracy of 0.5 μm through general-purpose

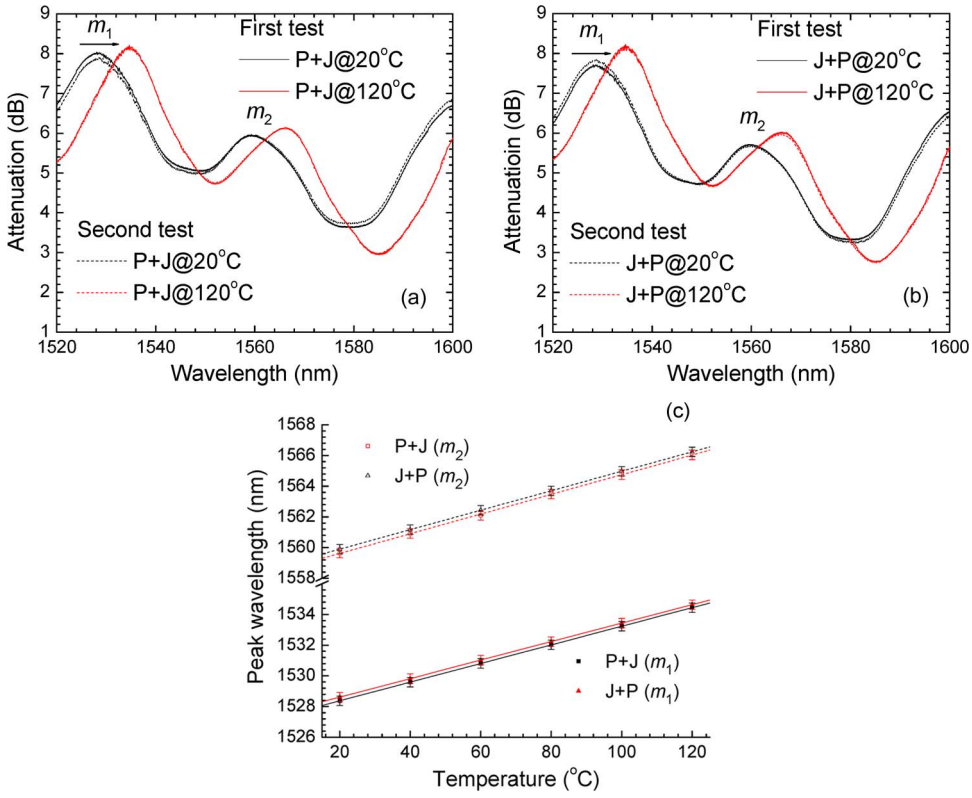

Fig. 6. Attenuation spectra of aFMZIs at different environmental temperatures. (a) P + J type, (b) J + P type, and (c) the dependences of the shifts in the attenuation peak wavelengths of the two types of aFMZI on temperature at different interference orders without strain.

interface bus system (GPIB) and LabVIEW programming control. In the initial temperature-sensing measurement, the environmental temperature was first increased from 20 °C to 120 °C with no strain applied on two types of aFMZIs, and after the first test, ambient temperature was cooled down to 20 °C, and a second test was carried out to investigate the stability and reproducibility of the fiber sensor. The corresponding attenuation peak wavelength shifts in the attenuation spectra are shown in Fig. 6(a) and (b). In the first test, two interference orders m_1 and m_2 for P + J type aFMZI with the attenuation peak wavelengths $\lambda_{m1,P+J}$ of 1528.38 nm and $\lambda_{m2,P+J}$ of 1559.64 nm at 20 °C are calculated to be 49 and 48, respectively. Two interference orders m_1 and m_2 for J + P type aFMZI show the attenuation peak wavelengths $\lambda_{m1,J+P}$ of 1528.62 nm and $\lambda_{m2,J+P}$ of 1559.9 nm at 20 °C, respectively. For the same interference order, the differences in the interferometer length ($l + l_0$ and l) and the effective refractive index induce a shift in the attenuation peak wavelength. The shift of the attenuation peak wavelength $\delta\lambda_{m,T}$ due to temperature increase can be expressed as

$$\delta\lambda_{m,T} = \frac{2(\Delta n_{\text{eff},T} + \delta n_{\text{eff},T})L}{2m+1} - \frac{2\Delta n_{\text{eff},T}L}{2m+1} = \frac{2\delta n_{\text{eff},T}L}{2m+1} \quad (1)$$

where $\delta n_{\text{eff},T}$ is the increased difference in the effective refractive index induced by the increase of the environmental temperature [13]. When the environmental temperature increases, the attenuation peak wavelength exhibits a redshift. The enhancement in the difference of the effective refractive index $\delta n_{\text{eff},T}$ is about 1.6×10^{-5} with a temperature increase of 100 °C at a wavelength of 1530.00 nm. For the P + J type aFMZI, the temperature sensitivities at the order m_1 and m_2 are 60.6 and 64.0 pm/°C (redshift), respectively. For the J + P type aFMZI, the temperature sensitivities at the order m_1 and m_2 are 60.2 and 63.4 pm/°C (redshift), respectively. In the second test, during the decreasing temperature, the temperature sensitivities at the order m_1 and m_2 are 60.2 and

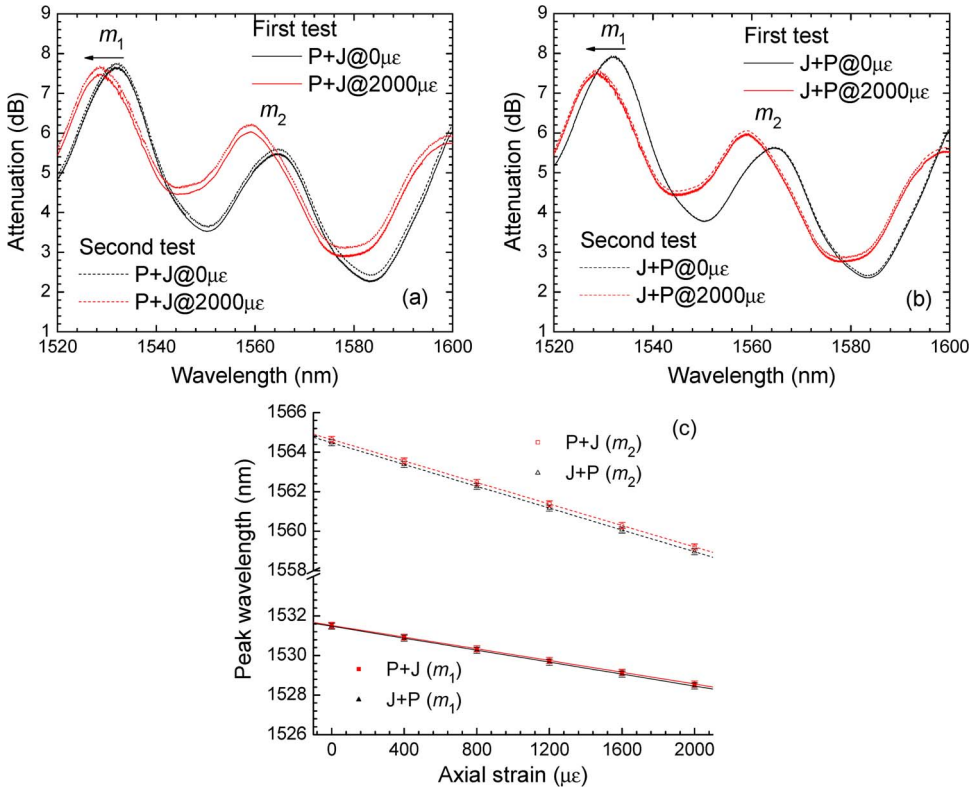

Fig. 7. Attenuation spectra of the aFMZIs under different axial strains. (a) P + J type, (b) J + P type, and (c) the dependences of the shifts in the attenuation peak wavelengths of the two types of aFMZI on axial strain at different interference orders at 20 °C.

63.8 pm/°C for the P + J type aFMZI and 59.9 and 63.2 pm/°C for the J + P type, respectively. Fig. 6(c) shows average dependences of the peak wavelength shifts of the two types of aFMZI for different interference orders on the temperature change. The sensing performance shows good stability and reproducibility with a standard deviation of 0.3% of the mean value of temperature sensitivities within the linear range from 20 °C to 100 °C. It is noted that the lower interference order m_2 shows a larger shift in the peak wavelength than that of the higher order m_1.

When an appropriate axial strain is applied on the two types of aFMZI kept at a constant temperature of 20 °C, the shifts in the attenuation spectra are shown in Fig. 7(a) and (b), as the axial strain is increased from 0 to 2000 $\mu\varepsilon$. In the first test during the increasing strain, two interference orders m_1 and m_2 for the P + J type aFMZI have the attenuation peak wavelengths $\lambda_{m1,\mathrm{P+J}}$ of 1531.52 nm and $\lambda_{m2,\mathrm{P+J}}$ of 1564.64 nm at 0 $\mu\varepsilon$, respectively, and the two interference orders m_1 and m_2 of the J + P type aFMZIs have the attenuation peak wavelengths $\lambda_{m1,\mathrm{J+P}}$ of 1531.48 nm and $\lambda_{m2,\mathrm{J+P}}$ of 1564.48 nm, respectively. The shift in the attenuation peak wavelength $\delta\lambda_{m,\varepsilon}$, due to the change in axial strain, can be expressed as

$$\delta\lambda_{m,\varepsilon} = \frac{2(\Delta n_{\mathrm{eff},\varepsilon} - \delta n_{\mathrm{eff},\varepsilon})(L+\delta L)}{2m+1} - \frac{2\Delta n_{\mathrm{eff},\varepsilon} L}{2m+1} \approx \frac{2(\Delta n_{\mathrm{eff},\varepsilon}\delta L - L\delta n_{\mathrm{eff},\varepsilon})}{2m+1} \tag{2}$$

where δL is the change in the interferometer length between P and J, and $\delta n_{\mathrm{eff},\varepsilon}$ is the change in the effective refractive index due to the increase of the external axial strain. The increase in the fiber length due to axial strain and the accompanying decreases in the radii of the fiber core and cladding result in a decrease in the normalized frequency V. More power is transferred to the fiber cladding from the core by mode coupling, and thus, the difference in the effective refractive indices between the core and the cladding modes reduces. The increase in the aFMZI length $\Delta n_{\mathrm{eff},\varepsilon}\delta L$ has

TABLE 1

Comparison of the performance of the reported Fiber Mach–Zehnder interferometers: —, Data not available; RI, Refractive index; MMF, Multimode fiber

Ref.	Fiber type	Interferometer structure	Fabrication technique	Measurands	Extinction ratio & Loss (device length)	Sensing performance	Direction dependence
[3]	SMF	Biconic taper	Heating-stretching	T, RI	—	$\Delta T \sim 1$ °C, $\Delta n \sim 1.42 \times 10^{-5}$	None
[7]	PCF	LPG pairs	Mechanical pressing with grooved plates onto a flat plate	—	4 dB & 4 dB	—	None
[8]	SMF	LPG-taper-LPG	LPG made by excimer laser, and taper made by stretching a fiber over a flame	RI	15 dB & 2 dB (12 mm)	49.4 nm/RIU	None
				RI	13 dB & 3 dB (16 mm)	173.8 nm/RIU	None
[9]	PCF	Core offset pairs	Cleaving and splicing using a fusion splicer	Strain	—	-2.16 pm/με (1487 nm), -2.28 pm/με (1560 nm)	None
		Collapsed air-holes	Electric arc of a fusion splicer	Strain			None
[10]	SMF	Core offset pairs	Fusion splicing	RI	13 dB & 10 dB (60 mm)	-33.3 nm/RIU (Michelson)	None
[11]	SMF	Taper pairs	Fusion splicing	RI	6 dB & 14.0 dB (55 mm)	-17.1 nm/RIU	None
[12]	SMF	Taper pairs	Fusion splicing	Strain	24 dB & 3 dB	2000 nm/ε	None
[13]	SMF	Taper pairs	Fusion splicing	RI & T	4 dB & 1 dB	-23.188 nm/RIU and 0.071 nm/°C (m_1) -26.087 nm/RIU and 0.077 nm/°C (m_2)	None
[14]	SMF	Single taper with air-glass reflection end	Fusion splicing	Flow velocity	—	69.8 deg/bar (compressed air pressure)	None
[15]	SMF	Single taper with gold coating reflection end	Fusion splicing	RI	13 dB & 1 dB	29 nm/RIU	None
[16]	SMF	Two points	CO_2 laser irradiation	T	20 dB & 10 dB (5 mm)	0.0817 nm/°C (5 mm)	None
[17]	SMF, MMF	MMF and LPG	Arc-induced LPG	Bending	13 dB & 8 dB	612.44 degrees.m	None
[18]	SMF	Taper and LPG	Taper by fusion splicing and arc-induced LPG	Rotation angle	1 dB & 2.5 dB	measure both the magnitude of the rotation angle and its sign.	None
[19]	SMF	Misaligned splicing point and LPG	Misaligned splicing point by fusion splicer and LPG by 244 nm laser	Strain & T	18 dB & 3 dB	59.1 pm/°C -0.6 pm/με	None
[20]	SMF, PCF	Misaligned splicing point and LPG	Misaligned splicing point by fusion splicer and LPG by mechanical pressing with grooved plates	—	8 dB & 7 dB	—	None
This study	SMF	Taper and lateral-shifted junction	Fusion splicing	Strain & T	4 dB & 4 dB	T+J 60.4 pm/°C and -1.47 pm/με (m_1) 63.9 pm/°C and -2.71 pm/με (m_2)	Versatile

a weaker impact on the peak wavelength shift than the influence of a decrease in the difference of the effective refractive indices $-L\delta n_{\text{eff},\varepsilon}$ so that the attenuation peak wavelength will blue-shift when the axial strain increases. The decrease in the difference of the effective refractive indices $\delta n_{\text{eff},\varepsilon}$ is calculated to be 1.1×10^{-5} with an increase in the axial strain of 2000 $\mu\varepsilon$ at a wavelength of 1530.00 nm. For the P + J type aFMZI, the strain sensitivities at the order m_1 and m_2 are -1.48 and -2.72 pm/$\mu\varepsilon$ (blueshift), respectively. For the J + P type aFMZI, the strain sensitivities at the order m_1 and m_2 are -1.51 and -2.76 pm/$\mu\varepsilon$ (blueshift), respectively. In the second test during the increasing strain, the axial strain sensitivities at the order m_1 and m_2 are -1.46 and -2.7 pm/$\mu\varepsilon$ for the P + J type aFMZI and -1.5 and -2.74 pm/$\mu\varepsilon$ for the J + P type, respectively. Fig. 7(c) shows the average dependences of the shifts in the peak wavelengths of the two types of aFMZI at different interference orders on the change in the axial strain. Compared with the attenuation peak wavelength of the higher interference order, the peak wavelength of the lower interference order exhibits larger axial strain sensitivity. In addition, the aFMZIs studied here show good stability and high reproducibility in the sensing performance. The difference in the interferometer length L between these two types of aFMZI is the taper length l_0 because the mode coupling takes place at the beginning of the entry part of the fiber taper. The effect of the subtle discrimination of the phase difference in the interferometer due to the multiplication of the effective refractive index and the interferometer length for these two types of aFMZI gives rise to different temperature and axial strain sensitivities. The interferometer proposed in this study offers the possibility to configure it either as a direction independent or dependent sensor for different device architectures. In the case when the taper and the lateral-shifted junction locate spatially close, the sensitivities of the interferometer can be tuned to be direction dependent. However, if the length of the taper is much smaller than the distance between the taper and the lateral-shifted junction, the sensitivities of the interferometer on the environmental parameters are not dependent on the configuration of the interferometer and, thus, are direction independent. In this case, the larger wavelength spacing resulted from the longer distance between the taper and the junction, as discussed in Fig. 4, may introduce inconvenience for the spectral measurement. With the specifications of the taper length and the interferometer length of the aFMZI adopted here, the sensitivity difference between the two types of aFMZIs is much smaller than that between different interference orders for the same type of aFMZI. It is obvious that different interference orders have different gradients of the peak wavelength on temperature and axial strain, even for the same type of aFMZI. We define a character matrix $M_{\varepsilon T(P+J)}$ composed of the mean temperature and axial strain sensitivities of the two tests at the orders m_1 and m_2 to represent the sensing performance of the P + J type aFMZI:

$$\begin{bmatrix} \Delta\lambda_{m1} \\ \Delta\lambda_{m2} \end{bmatrix}_{P+J} = M_{\varepsilon T(P+J)} \begin{bmatrix} \Delta T \\ \Delta\varepsilon \end{bmatrix} = \begin{bmatrix} 60.4 & -1.47 \\ 63.9 & -2.71 \end{bmatrix} \begin{bmatrix} \Delta T \\ \Delta\varepsilon \end{bmatrix} \tag{3}$$

which is equivalent to the following equation through a matrix transposition:

$$\begin{bmatrix} \Delta T \\ \Delta\varepsilon \end{bmatrix} = M^{-1}_{\varepsilon T(P+J)} \begin{bmatrix} \Delta\lambda_{m1} \\ \Delta\lambda_{m2} \end{bmatrix}. \tag{4}$$

A similar character matrix $M_{\varepsilon T(J+P)}$ for J + P type of the aFMZIs may also be used for simultaneous sensing of the two parameters:

$$\begin{bmatrix} \Delta\lambda_{m1} \\ \Delta\lambda_{m2} \end{bmatrix}_{J+P} = M_{\varepsilon T(J+P)} \begin{bmatrix} \Delta T \\ \Delta\varepsilon \end{bmatrix} = \begin{bmatrix} 60.1 & -1.51 \\ 63.3 & -2.75 \end{bmatrix} \begin{bmatrix} \Delta T \\ \Delta\varepsilon \end{bmatrix}. \tag{5}$$

In this case, once the character matrix is obtained through calibration, simultaneous measurement of axial strain and temperature can be achieved by reading the shifts in the attenuation peak wavelengths of the two types of aFMZI. A comparison between the FMZI developed in this study and other reported fiber interferometers is listed in Table 1, which indicates advantages of the aFMZI developed in this study including easy fabrication by a fusion splicer and low cost using a standard

single-mode telecommunication fiber, versatility in direction selection for the tunable sensing responses, and the possibility of multiparameter sensing. With regard to the practical applications of the aFMZI proposed in this study, as evident in Fig. 3(c), even though the mechanical strength of the tapered fiber decreases as compared with the standard single-mode fiber with coating, it is still possible to find a tapered fiber of suitable specifications to satisfy the requirement of axial strain measurement with an upper limit of 23×10^3 $\mu\varepsilon$. In fact, tapered fibers have been widely adopted for sensing based on surface plasmon resonance [21], despite the degradation in the mechanical strength. The fragility of a tapered fiber may result from either the axial or radial strain. For packaging method, the tapered fiber can be laid into a micromachined channel fabricated on a solid substrate (for example, a piece of glass) so that the radial strain can be avoided. In this case, the tapered region will not touch the channel due to the reduced diameter while the bottom of the rest fiber with coating will touch the channel in which no strain is induced. When an axial strain is applied on the device, the tapered fiber will be lifted up from the bottom of the microchannels with no contact.

4. Conclusion

In summary, we propose and demonstrate an approach to realize simultaneous measurement of axial strain and temperature using an aFMZI. The interferometer offers the possibility to tune its sensing performance, either direction dependent or independent, to satisfy requirements of specific applications. Furthermore, the asymmetrical structure of the interferometer with flexible device specifications, as well as its arbitrarily selectable interference orders, provides the feasibility to measure a large number of measurands with different sensitivities to environmental parameters, which make it possible to realize *in situ* multiple parameter measurement. This fiber interferometer presents a compact one-fiber solution for the measurement with the merits of simplicity in the sensing principle, high sensitivities, ease of fabrication, and low cost.

References

[1] M. G. Kuzyk, *Polymer Fiber Optics: Materials, Physics, and Applications*. Boca Raton, FL: CRC, 2006.

[2] L. Zhao, X. G. Tu, Y. H. Zuo, S. W. Chen, and Q. M. Wang, "Electro-optic coefficients of $Si_{0.75}Ge_{0.25}/Si/Si_{0.5}Ge_{0.5}$ asymmetric superlattice measured by polarization-maintaining fiber-optic Mach–Zehnder interferometer," *Appl. Phys. Lett.*, vol. 89, no. 14, pp. 141104-1–141104-3, Oct. 2006.

[3] K. Q. Kieu and M. Mansuripur, "Biconical fiber taper sensors," *IEEE Photon. Technol. Lett.*, vol. 18, no. 21, pp. 2239–2241, Nov. 2006.

[4] P. Chen, X. G. Tu, S. P. Li, J. C. Li, W. Lin, H. Y. Chen, D. Y. Liu, J. Y. Kang, Y. H. Zuo, L. Zhao, S. W. Chen, Y. D. Yu, J. Z. Yu, and Q. M. Wang, "Enhanced Pockels effect inGaN/$Al_xGa_{1-x}N$ superlattice measured by polarization-maintaining fiber Mach–Zehnder interferometer," *Appl. Phys. Lett.*, vol. 91, no. 3, pp. 031103-1–031103-3, Jul. 2007.

[5] D. K. Gramotnev and S. I. Bozhevolnyi, "Plasmonics beyond the diffraction limit," *Nat. Photon.*, vol. 4, no. 2, pp. 83–91, Feb. 2010.

[6] W. Z. Song, A. Q. Liu, S. Swaminathan, C. S. Lim, P. H. Yap, and T. C. Ayi, "Determination of single living cell's dry/water mass using optofluidic chip," *Appl. Phys. Lett.*, vol. 91, no. 22, pp. 223902-1–223902-3, Nov. 2007.

[7] J. H. Lim, H. S. Jang, K. S. Lee, J. C. Kim, and B. H. Lee, "Mach–Zehnder interferometer formed in a photonic crystal fiber based on a pair of long-period fiber gratings," *Opt. Lett.*, vol. 29, no. 4, pp. 346–348, Feb. 2004.

[8] J. F. Ding, A. P. Zhang, L. Y. Shao, J. H. Yan, and S. He, "Fiber-taper seeded long-period grating pair as a highly sensitive refractive-index sensor," *IEEE Photon. Technol. Lett.*, vol. 17, no. 6, pp. 1247–1249, Jun. 2005.

[9] H. Y. Choi, M. J. Kim, and B. H. Lee, "All-fiber Mach–Zehnder type interferometers formed in photonic crystal fiber," *Opt. Express*, vol. 15, no. 9, pp. 5711–5720, Apr. 2007.

[10] Z. Tian, S. S.-H. Yam, and H.-P. Loock, "Single-mode fiber refractive index sensor based on core-offset attenuators," *IEEE Photon. Technol. Lett.*, vol. 20, no. 16, pp. 1387–1389, Aug. 2008.

[11] Z. Tian, S. S.-H. Yam, J. Barnes, W. Bock, P. Greig, J. M. Fraser, H.-P. Loock, and R. D. Oleschuk, "Refractive index sensing with Mach–Zehnder interferometer based on concatenating two single-mode fiber tapers," *IEEE Photon. Technol. Lett.*, vol. 20, no. 8, pp. 626–628, Apr. 2008.

[12] Z. Tian and S. S.-H. Yam, "In-line abrupt taper optical fiber Mach–Zehnder interferometric strain sensor," *IEEE Photon. Technol. Lett.*, vol. 21, no. 3, pp. 161–163, Feb. 2009.

[13] P. Lu, L. Men, K. Sooley, and Q. Chen, "Tapered fiber Mach–Zehnder interferometer for simultaneous measurement of refractive index and temperature," *Appl. Phys. Lett.*, vol. 94, no. 13, pp. 131110-1–131110-3, Mar. 2009.

[14] O. Frazão, P. Caldas, F. M. Araújo, L. A. Ferreira, and J. L. Santos, "Optical flowmeter using a modal interferometer based on a single non-adiabatic fiber taper," *Opt. Lett.*, vol. 32, no. 14, pp. 1974–1976, Jul. 2007.

[15] Z. Tian, S. S.-H. Yam, and H. P. Loock, "Refractive index sensor based on an abrupt taper Michelson interferometer in a single-mode fiber," *Opt. Lett.*, vol. 33, no. 10, pp. 1105–1107, May 2008.

[16] W. Tao, X. Lan, and H. Xiao, "Fiber inline core-cladding-mode Mach–Zehnder interferometer fabricated by two-point CO_2 laser irradiations," *IEEE Photon. Technol. Lett.*, vol. 21, no. 10, pp. 669–671, May 2009.
[17] O. Frazão, J. Viegas, P. Caldas, J. L. Santos, F. M. Araújo, L. A. Ferreira, and F. Farahi, "All-fiber Mach–Zehnder curvature sensor based on multimode interference combined with a long-period grating," *Opt. Lett.*, vol. 32, no. 21, pp. 3074–3076, Nov. 2007.
[18] O. Frazão, R. Falate, J. L. Fabris, J. L. Santos, L. A. Ferreira, and F. M. Araújo, "Optical inclinometer based on a single long-period fiber grating combined with a fused taper," *Opt. Lett.*, vol. 31, no. 20, pp. 2960–2962, Nov. 2006.
[19] X. Dong, L. Su, P. Shum, Y. Chung, and C. C. Chan, "Wavelength-selective all-fiber filter based on a single long-period fiber grating and a misaligned splicing point," *Opt. Commun.*, vol. 258, no. 2, pp. 159–163, Feb. 2006.
[20] X. Yu, P. Shum, and X. Dong, "Photonic-crystal-fiber-based Mach–Zehnder interferometer using long-period gratings," *Microw. Opt. Technol. Lett.*, vol. 48, no. 7, pp. 1379–1383, Jul. 2006.
[21] Y.-C. Kim, W. Peng, S. Banerji, and K. S. Booksh, "Tapered fiber optic surface plasmon resonance sensor for analyses of vapour and liquid phases," *Opt. Lett.*, vol. 30, no. 17, pp. 2218–2220, Sep. 2005.